Proceedings of the ASME 2014 Dynamic Systems and Control Conference
DSCC 2014
October 22-24, 2014, San Antonio, TX, USA

DSCC2014-6254

BATTERY STATE OF HEALTH MONITORING BY SIDE REACTION CURRENT DENSITY ESTIMATION VIA RETROSPECTIVE-COST SUBSYSTEM IDENTIFICATION

Xin Zhou
Department of Mechanical Engineering
University of Michigan
Ann Arbor, MI, 48109
Email: zhouxin@umich.edu

Tulga Ersal
Department of Mechanical Engineering
University of Michigan
Ann Arbor, MI, 48109
Email: tersal@umich.edu

Jeffrey L. Stein
Department of Mechanical Engineering
University of Michigan
Ann Arbor, MI, 48109
Email: stein@umich.edu

Dennis S. Bernstein
Department of Aerospace Engineering
University of Michigan
Ann Arbor, MI, 48109
Email: dsbaero@umich.edu

ABSTRACT

This paper introduces a method to estimate battery state of health (SoH) via health-relevant electrochemical features. Battery state of health estimation is a critical part of battery management because it allows for balancing the trade-off between maximizing performance and minimizing degradation. In this paper, a health-relevant electrochemical feature, the side reaction current density, is used as the indicator of battery SoH. An estimation algorithm is required due to the unavailability of the side reaction current density via noninvasive methods. In this paper, Retrospective-Cost Subsystem Identification (RCSI) is used to estimate the side reaction current density via identification of an unknown battery health subsystem that generates the side reaction current density. Simulation results are provided for constant current charge and discharge cycles with different C rates. A current profile for an electric vehicle (EV) going through Urban Dynamometer Driving Schedule (UDDS) cycles is also used as the excitation signal during estimation. The simulations show promising results in battery health dynamic identification and side reaction current density estimation with RCSI.

NOMENCLATURE

j Electrode name, where p stands for the cathode and n stands for the anode.

c_s Li-ion concentration in the solid phase. $[mol/m^3]$
c_{se} Solid-electrolyte interface Li-ion concentration. $[mol/m^3]$
$J_{1,j}$ Intercalation current density. $[A/m^3]$
J_j Total current density. $[A/m^3]$
J_{sd} Side reaction current density. $[A/m^3]$
$\phi_{e,j}$ Potential of electrolyte phase. $[V]$
$\phi_{s,j}$ Potential of solid phase. $[V]$
R_j Radius of electrodes. [m]
D_s Diffusion coefficient in solid phase. $[m^2/sec^3]$
κ^{eff} Conductivity of electrolyte. $[S/m]$
σ^{eff} Conductivity of solid phase. $[S/m]$
$a_{s,j}$ Specific surface area of porous electrodes. $[1/m^3]$
$i_{0,j}$ Intercalation exchange-current density. $[A/m^2]$
η_j Overpotential for intercalation reaction.$[V]$
$\alpha_{a,j}$ Anodic transfer coefficients of electrochemical reaction.
$\alpha_{c,j}$ Cathodic transfer coefficients of electrochemical reaction.
F Faraday constant. 96487 $[C/mol]$
R Universal gas constant. 8.314 $[J/mol]$
T Temperature. $[K]$
$U_{ref,j}$ Equilibrium potential of intercalation reaction. $[V]$
R_{film} SEI film resistance. $[\Omega m^2]$
A Total area of the electrode. $[m^2]$

δ_j Total length of the electrode or separator. $[m]$
$i_{0,sd}$ Side reaction exchange-current density. $[A/m^2]$
$J_{sd,n}$ Side reaction current density in the anode. $[A/m^3]$
η_{sd} Overpotential for side reaction. $[V]$
$U_{ref,sd}$ Equilibrium potential of side reaction. $[V]$

INTRODUCTION

Battery State of Health (SoH) is a critical input to the battery management system because it allows for balancing the trade-off between maximizing performance and minimizing degradation. However, battery SoH is not a quantity that can be directly measured, thus it would be beneficial to estimate battery SoH from only commonly available measurements: terminal voltage, current and temperature. The research about SoH estimation contains three basic components: i) a SoH indicator that is correlated with battery health; ii) a model that represents the relationship between the SoH indicator and terminal voltage, current and temperature; iii) an estimation algorithm that can estimate the SoH indicator from the measurements. The contribution of this paper is using an existing estimation algorithm for the first time to estimate the side reaction current density as an indicator of battery SOH.

The knowledge of battery degradation mechanisms is essential when selecting SoH indicator. Most electrochemical-based degradation mechanisms are irreversible side reactions which cause changes in battery electrochemical features and express themselves as a reduction in capacity (capacity fade) and power (power fade), the later due to an increase in the effective internal battery resistance. Side reactions consume the cyclable Li-ions in the battery and lead to capacity fade [1]. Some side reactions also produce by-products. For example, one important degradation mechanism for $LiFePO_4$ battery is the solid-electrolyte interface (SEI) film formation. The deposit produced by the side reaction increases the SEI film thickness and leads to increasing internal resistance [2].

Based on the selection of the SoH indicator, the literature in SoH estimation can be divided into two categories. Most of the literature uses the degradation effects as the SoH indicator. The capacity is identified using extended Kalman filter as a parameter in empirical battery models [3–5]. The internal resistance is estimated using central difference Kalman filter as the parameter in a LTV model [6]. Equivalent circuit models or other empirical models are often sufficient for these applications as the mapping between SoH indicator and the voltage, current and temperature. The simplicity of these models is the key advantage. However, these degradation effects can be inaccurate in representing the SoH. This is because these effects are not only related to the battery SoH, but are also influenced by environmental conditions and use patterns [7].

The second category uses the electrochemical features as the SoH indicator. The benefit of using these features is that they can uniquely indicate the level of degradation of battery regardless of the environmental conditions and use patterns. Cyclable Li-ions is identified using an adaptive PDE observer with nonlinear least squares [8]. SEI film resistance is estimated using retrospective-cost subsystem identification [9, 10].

In this paper, an alternative battery electrochemical feature, the side reaction current density, is selected as the SoH indicator. The side reaction current density is a battery electrochemical feature that measures the rate for cyclable Li-ion consumption, which contributes to battery capacity fade [1], in all degradation mechanisms that are caused by side reactions.

The main challenges of using the electrochemical features as the SoH indicator are that i) the electrochemical features are only available from invasive and/or destructive methods; ii) to estimate the electrochemical features always requires the use of electrochemical model of a battery. The large complexity of the model can make accurate estimation challenging.

In this paper, a method is presented to address the two challenges. To address the first challenge, the battery health system is treated as an inaccessible subsystem of the whole battery system. Then Retrospective-Cost Subsystem Identification (RCSI) [11,12] is used to identify the subsystem and estimate the battery health-relevant electrochemical features. A few model simplification and approximation methods are used to deal with the second challenge.

This paper has its novelty compared to [8–10] in the following two aspects. First, in this paper the side reaction current density is used as the SoH indicator instead of cyclable Li-ions [8] or SEI film resistance [9, 10]. The benefits of using the side reaction current density as the SoH indicator are as follows. i) The side reaction current density measures the rate of Li-ion loss, which can be more sensitive than the direct identification of the cyclable Li-ions itself, given the amount of cyclable Li-ion loss can be very small compared to the total number of Li-ions. ii) Compared to the SEI film resistance that can apply only when the side reaction mainly causes SEI film formation, the side reaction current density can be used as the SoH indicator for all side-reaction-related degradation. iii) Only one parameter, the gain of the subsystem model (battery health model), needs to be identified in order to estimate the side reaction current density. However, a dynamic system has to be identified to estimate the SEI film resistance [9, 10]. In this paper, subsystem parameter can be successfully identified under certain conditions, while in [9, 10] the subsystem parameters are not correctly identified. The linearity of the subsystem model also allows the application in the combination of several degradation mechanisms. The second novelty is in the RCSI algorithm. In the updating algorithm part of RCSI, Kalman filter is used instead of Recursive Least Squares in [9, 10]. Experiments show that this change allows faster and more accurate convergence in the application in this paper.

The rest of the paper is organized as follows. The first

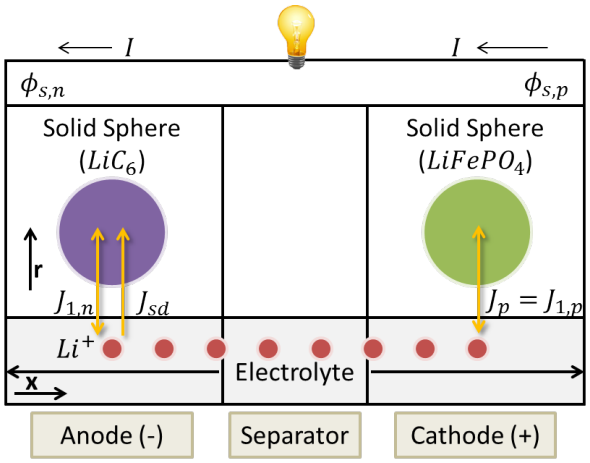

FIGURE 1. Li-ion cell schematic using single particle model. The single particle model use one representative sphere particle to represent each electrode.

section introduces the development of the electrochemical-based control model. The features of the battery model are highlighted. The second section discusses the retrospective-cost subsystem identification (RCSI) and its application to the battery. Simulation results and discussion are given in the following section. The conclusion is given in the final section.

BATTERY MODEL

The battery model acts as the map relating the SoH indicator, here the side reaction current density, to the measurable quantities, here voltage and current. This relationship is contained in the battery charge and discharge dynamics. Use of electrochemical features as the SoH indicator makes the electrochemical model a necessary choice for the battery model in this paper.

The results in this paper are simulation-based, thus a representation of the true battery degradation system is in need. A battery charge and discharge model is augmented with an electrochemical degradation model to represent the true battery system. The output of the degradation model is the SoH indicator, the side reaction current density.

In this section the battery model is discussed. The electrochemical governing equations are introduced first, followed by the control model developed from the stated electrochemical model. Some features of the model from the perspective of control and estimation are highlighted.

Electrochemical Battery Model

Battery Charge and Discharge Model Unlike [9,10] where the Doyle Fuller Newman (DFN) model [13] was used as the battery charge and discharge model, in this paper a simplified version of DFN model, namely the single particle model [14] is adopted.

Fig. 1 shows the Li-ion cell schematic with the single particle model. In the single particle model, each electrode is represented with one spherical particle.

The diffusion of lithium-ions inside the electrode particles are governed by Fick's law in spherical coordinates

$$\frac{\partial c_s}{\partial t} = \overrightarrow{\nabla}_r (D_s \overrightarrow{\nabla}_r c_s). \tag{1}$$

with the Neumann boundary condition

$$\left.\frac{\partial c_s}{\partial r}\right|_{r=0} = 0, \qquad \left.\frac{\partial c_s}{\partial r}\right|_{r=R_j} = -\frac{J_{1,j}}{F a_{s,j} D_s}. \tag{2}$$

The exchange of Li-ions between the solid electrode and electrolyte, namely the intercalation reaction, is the process that the battery stores and releases the energy and electricity. The intercalation reaction is governed by the Butler-Volmer equation

$$J_{1,j} = a_{s,j} i_{0,j} \left[\exp\left(\frac{\alpha_{a,j} F}{RT}\eta_j\right) - \exp\left(-\frac{\alpha_{c,j} F}{RT}\eta_j\right) \right], \tag{3}$$

where

$$\eta_p = \phi_{p,s} - \phi_{p,e} - U_{ref,p}, \tag{4}$$

$$\eta_n = \phi_{n,s} - \phi_{n,e} - U_{ref,n} - \frac{J_n}{a_{s,n}} R_{film}. \tag{5}$$

The $J_{1,j}$ in Eq. (3) represents the intercalation current density. The intercalation reaction is a reversable reaction and $J_{1,j}$ reflects the cyclable Li-ions inside the battery.

The distribution of the potential along the thickness of the anode-separator-cathode sandwich is governed by the equation

$$\overrightarrow{\nabla}_x \kappa^{eff} \overrightarrow{\nabla}_x \phi_{e,j} = -J_j, \tag{6}$$

$$\overrightarrow{\nabla}_x \sigma^{eff} \overrightarrow{\nabla}_x \phi_{s,j} = J_j. \tag{7}$$

Health Model Arora model [1] is selected to act as the true health system in simulation. This model is suitable for all electrochemical-based degradation mechanisms that contributes to side reaction current density. While the health model in [9,10] adopted from [2] is a specific example of this model in the solid-electrolyte interface film formation mechanism.

The degradation is modelled with irreversible side reaction. The side reaction affects the charge and discharge dynamics by taking away the useful intercalation current density. The cyclable Li-ion consumption causes the capacity fade of the battery.

$$J_j = J_{1,j} + J_{sd,j} \tag{8}$$

In the model, the degradation is assumed to happen only in the anode. Thus,

$$J_{sd,p} = 0; \tag{9}$$

while the side reaction in the anode is governed by Butler-Volmer equation,

$$J_{sd,n} = -i_{0,sd} a_{s,n} \exp\left(-\frac{\alpha_{c,n} F}{RT}\eta_{sd}\right), \tag{10}$$

where

$$\eta_{sd} = \phi_s - \phi_e - U_{ref,sd} - \frac{J_n}{a_{s,n}} R_{film}, \tag{11}$$

Control Model Development

This section introduces the state space form of the battery model. In this paper, only the current driving mode is considered based on the conclusion of [9, 10] where the identification is accurate only in constant charge mode when the side reaction is significant.

The input of the system is current, and the discharge current is assumed to be the positive direction.

$$J_n = \frac{I}{A\delta_n}, \tag{12}$$

$$J_p = -\frac{I}{A\delta_p}. \tag{13}$$

The state equation is a state space realization of the second order Padé Approximation of the transfer function from the Laplace transformation of (1) [15]. Assuming a sampling time of T_s, first order hold discretization of the continuous state space equation yields

$$A_j = \begin{bmatrix} 1 & 0 \\ 0 & e^{-\frac{35D_{s,j}T_s}{R_j^2}} \end{bmatrix}, \tag{14}$$

$$B_j = \begin{bmatrix} \frac{R_j^2 T_s}{35D_{s,j}} \\ \frac{e^{-\frac{70D_{s,j}T_s}{R_j^2}} \left(-1+e^{\frac{35D_{s,j}T_s}{R_j^2}}\right)^2 R_j^4}{1225{D_{s,j}}^2 T_s} \end{bmatrix}, \tag{15}$$

$$C_j = \begin{bmatrix} -\frac{105{D_{s,j}}^2 m_j}{R_j^3} & -\frac{7D_{s,j}m_j}{R_j} \end{bmatrix}, \tag{16}$$

$$D_j = \begin{bmatrix} \frac{m_j\left(\left(2-2e^{-\frac{35D_{s,j}T_s}{R_j^2}}\right)R_j^4 - 70D_{s,j}R_j^2T_s - 525D_s^2T_s^2\right)}{350D_{s,j}R_jT_s} \end{bmatrix}. \tag{17}$$

The input to Eq. (14 - 17) is $J_{1,j}$. Thus the input to the anode can be divided into the exogenous input J_j and the feedback signal from the health model $J_{sd,n}$.

The state equation for the battery charge and discharge system is obtained by stacking the matrix for the two electrodes. Notice that these two electrodes are uncoupled. From the A matrix, two of the eigenvalues of the system is at the unit circle, therefore the initialization errors in system states do not die down.

The output of the system is voltage, namely the potential difference between the solid phase of the two electrodes. The output equation is obtained by solving Eq. (3, 6 and 7). Without consideration of degradation, the solution for voltage is [16],

$$\begin{aligned} V = {} & U_{ref,p}(c_{se,p}) - U_{ref,n}(c_{se,n}) + \frac{RT}{\alpha F}\ln\left(\xi_p(c_{se,p},I) + \sqrt{\xi_p^2+1}\right) \\ & - \frac{RT}{\alpha F}\ln\left(\xi_n(c_{se,n},I) + \sqrt{\xi_n^2+1}\right) - \frac{I(k)}{A\delta_n a_{s,n}} R_{film} \\ & - \frac{I}{2A}\left(\frac{\delta_n}{\kappa_{eff,n}} + 2\frac{\delta_{sep}}{\kappa_{eff,sep}} + \frac{\delta_p}{\kappa_{eff,p}}\right). \end{aligned} \tag{18}$$

When the degradation in the anode is taken into consideration, the potential difference in the anode is defined as $d\phi_n = \phi_{n,s} - \phi_{n,e} - \frac{J_n}{a_{s,n}} R_{film}$. Then the terms related to anode Butler-Volmer equation and reference potential is replaced with $d\phi_n$.

As in [16], the reaction is assumed completely reversible, $\alpha_c = \alpha_a = 0.5$. By plugging Eq. (5) and (4) into Eq. (3),

$$\begin{aligned} J_{1,n} = {} & \frac{a_{s,n}i_{0,n}}{\exp\left(\frac{\alpha F}{RT}U_{ref,n}\right)} \frac{1}{\exp\left(-\frac{\alpha F}{RT}d\phi_n\right)} \\ & - a_{s,n}i_{0,n}\exp\left(\frac{\alpha F}{RT}U_{ref,n}\right)\exp\left(-\frac{\alpha F}{RT}d\phi_n\right). \end{aligned} \tag{19}$$

Eq. (10) can be written similarly,

$$J_{sd,n} = -i_{0,sd}a_{s,n}\exp\left(\frac{\alpha F}{RT}U_{ref,sd}\right)\exp\left(-\frac{\alpha F}{RT}d\phi_n\right). \tag{20}$$

Along with Eq. (8) in the anode, $J_{1,n}$, $J_{sd,n}$ and the solid phase potential in the anode can be solved.

Define the lumped parameters,

$$\begin{aligned} k_1 &= \frac{a_{s,n}i_{0,n}}{\exp\left(\frac{\alpha F}{RT}U_{ref,n}\right)}, \\ k_2 &= -a_{s,n}i_{0,n}\exp\left(\frac{\alpha F}{RT}U_{ref,n}\right), \\ k_3 &= -i_{0,sd}a_{s,n}\exp\left(\frac{\alpha F}{RT}U_{ref,sd}\right), \\ k_4 &= J_n. \end{aligned}$$

Solve for the exponential function of solid phase potential in the anode,

$$y(\phi) \triangleq \exp\left(-\frac{\alpha F}{RT}d\phi_n\right) = \frac{k_4 - \sqrt{k_4^2 - 4k_1(k_2+k_3)}}{2(k_2+k_3)}. \tag{21}$$

Thus,

$$d\phi_n = -\frac{RT}{\alpha F}\ln(y(\phi)). \tag{22}$$

The output equation is

$$\begin{aligned} V = {} & U_{ref,p}(c_{se,p}) + \frac{RT}{\alpha F}\ln\left(\xi_p(c_{se,p},I) + \sqrt{\xi_p^2+1}\right) + d\phi_n \\ & - \frac{1}{2A}\left(\frac{\delta_n}{\kappa_{eff,n}} + 2\frac{\delta_{sep}}{\kappa_{eff,sep}} + \frac{\delta_p}{\kappa_{eff,p}}\right)I - \frac{I(k)}{A\delta_n a_{s,n}}R_{film}. \end{aligned} \tag{23}$$

Also, the side reaction current density can be computed as a linear function of $y(\phi)$,

$$J_{sd,n} = k_3 y(\phi). \tag{24}$$

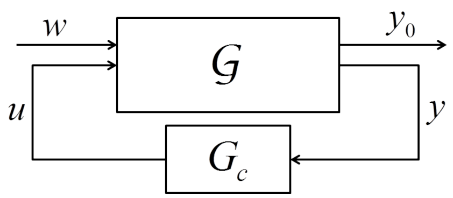

FIGURE 2. The standard feedback form. The feedback block is an inaccessible subsystem in the whole system.

The system above is a state space system with a linear state equation and a nonlinear output map. This is then put into standard feedback form as shown in Fig. 2. In the battery model, the signals are defined as follows: i) exogenous input w is defined to be current; ii) the feedback signal u is defined to be the side reaction current density; iii) the measurable output signals y_0 and unmeasurable output signal y are defined to be voltage and $y(\phi)$, respectively. Here the feedback block is the inaccessible degradation subsystem that needs to be estimated.

The state space form for $\mathscr{G}$ in battery system is

$$x(k+1) = Ax(k) + Bu(k) + Fw(k), \tag{25}$$

$$y(k) = f(x(k), u(k), w(k)), \tag{26}$$

$$y_0(k) = f_0(x(k), u(k), w(k)), \tag{27}$$

where A, B, F is the battery dynamics Eq. (3). $x(k) \in \mathbb{R}^n$ is the internal states of the battery model. $f(\cdot)$ and $f_0(\cdot)$ are the static relationship represented by Eq. (21) and (23).

The subsystem is a linear static equation.

$$u(k) = Ky(k), \tag{28}$$

where the linear gain K in Eq. (28) is k_3 in Eq. (24). Thus the true subsystem is a linear time invariant static equation.

REROSPECTIVE-COST SUBSYSTEM IDENTIFICATION

Fig. 3 presents the Retrospective-Cost Subsystem Identification architecture and its application to the battery. The upper block is the true system which contains a known main system and an unknown subsystem. The subsystem output is the inaccessible signal that needs to be estimated. In the battery application, main system is represented with Eq. (25) to (27); while the subsystem is represented with Eq. (28) where k_3 is assumed unknown. The lower block is the model of the true system. The main system model is built based on the knowledge of the main system. The form of the subsystem is assumed to be a mathematical approximation of the true subsystem form. The error between the output of the system and the subsystem model is computed and used to estimate the subsystem parameter and thus estimate the subsystem output. In the battery application, the main system is the battery charge and discharge dynamics that is assumed known. The unknown subsystem is the battery health system that needs to be estimated. The input and the output of the system are current and voltage respectively. The subsystem output is side reaction current density, the selected electrochemical-based SoH indicator.

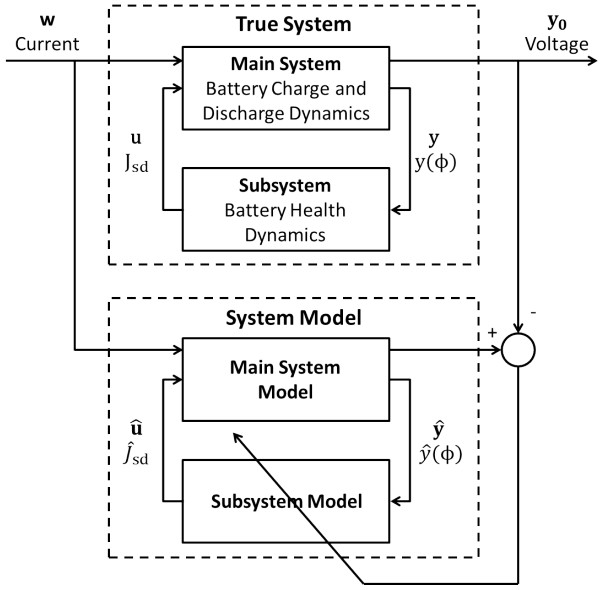

FIGURE 3. RCSI architecture in battery case.

In [9, 10], two step Recursive Least Squares version of Retrospective-Cost Subsystem Identification (RCSI) [11] is used to estimate the film resistance. In this paper, the two step Kalman Filter version of RCSI is used to estimate the side reaction current density. There are several other versions of RCSI, but this version is chosen because it converges the fastest in this application.

Retrospective Cost-Based Signal Construction

The true battery SISO system has the form as shown in Eq. (25 - 28). Now, construct a model of the true system

$$\hat{x}(k+1) = \hat{A}\hat{x}(k) + \hat{B}\hat{u}(k) + \hat{F}w(k), \tag{29}$$

$$\hat{y}(k) = \hat{f}(\hat{x}(k), \hat{u}(k), w(k)), \tag{30}$$

$$\hat{y}_0(k) = \hat{f}_0(\hat{x}(k), \hat{u}(k), w(k)), \tag{31}$$

$$z(k) = \hat{y}_0(k) - y_0(k), \tag{32}$$

where $\hat{x}(k) \in \mathbb{R}^n$, $\hat{y}(k) \in \mathbb{R}^{l_y}$, $z(k) \in \mathbb{R}^{l_z}$, $\hat{y}_0(k) \in \mathbb{R}^{l_{y_0}}$, $\hat{u}(k) \in \mathbb{R}^{l_u}$.

Let $\hat{E}_1\hat{x}(k) + \hat{E}_2\hat{u}(k) + \hat{E}_3\hat{w}(k)$ be the linear counterparts of $\hat{f}_0(\hat{x}(k), \hat{u}(k), \hat{w}(k))$. For $G_{y_0,u}$ and $i \geq 0$, define the Markov parameter

$$\hat{H}_i \triangleq \begin{cases} \hat{E}_2, & i = 0 \\ \hat{E}_1\hat{A}^{i-1}\hat{B}, & i \geq 1 \end{cases}. \tag{33}$$

Let r be a positive integer. Then, for all $k \geq r$,

$$\hat{x}(k) = \hat{A}^r\hat{x}(k-r) + \sum_{i=1}^{r} \hat{A}^{i-1}\hat{B}\hat{u}(k-i) + \sum_{i=1}^{r} \hat{A}^{i-1}\hat{F}w(k-i), \tag{34}$$

and thus

$$z(k) = \hat{E}_1\hat{A}^r\hat{x}(k-r) + \hat{E}_3 w(k) + \sum_{i=1}^{r} \hat{E}_1\hat{A}^{i-1}\hat{F}w(k-i) - y_0(k) + \bar{H}\bar{U}(k-1), \quad (35)$$

where

$$\bar{H} \triangleq \begin{bmatrix} H_0 & \cdots & H_r \end{bmatrix} \in \mathbb{R}^{l_z \times r l_u},$$
$$\bar{U}(k-1) \triangleq \begin{bmatrix} \hat{u}^{\mathrm{T}}(k) & \cdots & \hat{u}^{\mathrm{T}}(k-r) \end{bmatrix}^{\mathrm{T}}.$$

Next, rearrange the columns of $\bar{H}$ and the components of $\bar{U}(k-1)$ and partition the resulting matrix and vector so that

$$\bar{H}\bar{U}(k-1) = \mathscr{H}'U'(k-1) + \mathscr{H}U(k-1), \quad (36)$$

where $\mathscr{H}' \in \mathbb{R}^{l_z \times (r l_u - l_U)}$, $\mathscr{H} \in \mathbb{R}^{l_z \times l_U}$, $U'(k-1) \in \mathbb{R}^{r l_u - l_U}$, and $U(k-1) \in \mathbb{R}^{l_U}$. Then, (35) can be rewritten as

$$z(k) = \mathscr{S}(k) + \mathscr{H}U(k-1), \quad (37)$$

where

$$\mathscr{S}(k) \triangleq \hat{E}_1\hat{A}^r\hat{x}(k-r) + \hat{E}_3 w(k) + \sum_{i=1}^{r} \hat{E}_1\hat{A}^{i-1}\hat{F}w(k-i) - y_0(k) + \mathscr{H}'U'(k-1). \quad (38)$$

Next, rewrite (37) with a delay of k_j time steps, where $0 \leq k_1 \leq k_2 \leq \cdots \leq k_s$, in the form

$$z(k-k_j) = \mathscr{S}_j(k-k_j) + \mathscr{H}_j U_j(k-k_j-1), \quad (39)$$

where (38) becomes

$$\mathscr{S}_j(k-k_j) \triangleq \hat{E}_1\hat{A}^r\hat{x}(k-k_j-r) + \sum_{i=1}^{r} \hat{E}_1\hat{A}^{i-1}\hat{F}w(k-k_j-i) + \hat{E}_3 w(k-k_j) - y_0(k-k_j) + \mathscr{H}'_j U'_j(k-k_j-1) \quad (40)$$

and (36) becomes

$$\bar{H}\bar{U}(k-k_j-1) = \mathscr{H}'_j U'_j(k-k_j-1) + \mathscr{H}_j U_j(k-k_j-1), \quad (41)$$

where $\mathscr{H}'_j \in \mathbb{R}^{l_z \times (r l_u - l_{U_j})}$, $\mathscr{H}_j \in \mathbb{R}^{l_z \times l_{U_j}}$, $U'_j(k-k_j-1) \in \mathbb{R}^{r l_u - l_{U_j}}$, and $U_j(k-k_j-1) \in \mathbb{R}^{l_{U_j}}$.

Now, by stacking $z(k-k_1), \ldots, z(k-k_s)$, define the *extended performance*

$$Z(k) \triangleq \begin{bmatrix} z^{\mathrm{T}}(k-k_1) & \cdots & z^{\mathrm{T}}(k-k_s) \end{bmatrix}^{\mathrm{T}} \in \mathbb{R}^{s l_z}. \quad (42)$$

Therefore,

$$Z(k) \triangleq \tilde{\mathscr{S}}(k) + \tilde{\mathscr{H}}\tilde{U}(k-1), \quad (43)$$

where

$$\tilde{\mathscr{S}}(k) \triangleq \begin{bmatrix} \mathscr{S}(k-k_1) & \cdots & \mathscr{S}(k-k_s) \end{bmatrix}^{\mathrm{T}} \in \mathbb{R}^{s l_z}, \quad (44)$$

$\tilde{\mathscr{H}} \in \mathbb{R}^{s l_z \times l_{\tilde{U}}}$, and $\tilde{U}(k-1) \in \mathbb{R}^{l_{\tilde{U}}}$. The vector $\tilde{U}(k-1)$ is formed by stacking $U_1(k-k_1-1), \ldots, U_s(k-k_s-1)$ and removing repetitions of components. The coefficient matrix $\tilde{\mathscr{H}}$ consists of the entries of $\mathscr{H}_1, \ldots, \mathscr{H}_s$ arranged according to the structure of $\tilde{U}(k-1)$. Furthermore, it is assumed that the last entry of $\tilde{U}(k-1)$ is a component of $\hat{u}(k-r)$.

Next, define the *retrospective performance*

$$z(k-k_j)^* \triangleq \mathscr{S}_j(k-k_j) + \mathscr{H}_j U_j^*(k-k_j-1), \quad (45)$$

where the actual past subsystem outputs $U_j(k-k_j-1)$ in (39) are replaced by the surrogate subsystem outputs $\hat{U}_j^*(k-k_j-1)$.

The *extended retrospective performance* for (45), defined as

$$Z^*(k) \triangleq \begin{bmatrix} z^{*\mathrm{T}}(k-k_1) & \cdots & z^{*\mathrm{T}}(k-k_s) \end{bmatrix}^{\mathrm{T}} \in \mathbb{R}^{s l_z}, \quad (46)$$

is given by

$$Z^*(k) = \tilde{\mathscr{S}}(k) + \tilde{\mathscr{H}}\tilde{U}^*(k-1), \quad (47)$$

where the components of $\tilde{U}^*(k-1) \in \mathbb{R}^{l_{\tilde{U}^*}}$ are components of $\hat{U}_1^*(k-k_1-1), \ldots, \hat{U}_s^*(k-k_s-1)$ ordered in the same way as the components of $\tilde{U}^*(k-1)$. Subtracting (43) from (47) yields

$$Z^*(k) = Z(k) - \tilde{\mathscr{H}}\tilde{U}(k-1) + \tilde{\mathscr{H}}\tilde{U}^*(k-1). \quad (48)$$

Finally, define the *retrospective cost function*

$$\bar{J}(k) \triangleq Z^{*\mathrm{T}}(k)R_Z(k)Z^*(k) + \tilde{U}^{*\mathrm{T}}(k)R_U(k)\tilde{U}^*(k), \quad (49)$$

where $R_Z(k) \in \mathbb{R}^{l_z \times l_z}$ and $R_U(k) \in \mathbb{R}^{l_u \times l_u}$ are positive-definite performance weightings. The goal is to determine refined subsystem outputs $\hat{\tilde{U}}(k)$ that would have provided better performance than the subsystem model outputs $\hat{U}(k)$ that were applied to the system. The refined subsystem output values $\hat{\tilde{U}}(k)$ are subsequently used to update the subsystem estimate.

The unique global minimizer of Eq. (49) is

$$\tilde{U}^*(k) = -\frac{1}{2}\mathscr{A}^{-1}(k)\mathscr{B}(k), \quad (50)$$

where

$$\mathscr{A}(k) \triangleq \tilde{\mathscr{H}}^{\mathrm{T}}R_Z(k)\tilde{\mathscr{H}} + R_U(k), \quad (51)$$

$$\mathscr{B}(k) \triangleq 2\tilde{\mathscr{H}}^{\mathrm{T}}R_Z(k)[Z(k) - \tilde{\mathscr{H}}\tilde{U}(k-1)]. \quad (52)$$

Subsystem Modeling

The estimated subsystem output $\hat{u}(k)$ is given by a linear static gain given by

$$\hat{u}(k) = \hat{K}\hat{y}(k), \quad (53)$$

where $\hat{K}$ is an estimate of K.

The subsystem output (53) can be expressed in a standard ARMAX form

$$\hat{u}(k) = \theta(k)^{\mathrm{T}}\phi(k), \quad (54)$$

where $\theta(k) \in \mathbb{R}^{l_u \times l_y}$ is the parameter of the subsystem,

$$\theta(k) \triangleq [K]^{\mathrm{T}}; \quad (55)$$

and $\phi(k-1) \in \mathbb{R}^{1 \times l_y}$ is given by

$$\phi(k) \triangleq \begin{bmatrix} \hat{y}^{\mathrm{T}}(k) \end{bmatrix}^{\mathrm{T}}. \quad (56)$$

Kalman Filter Update

The Kalman filter updating law for the ARMAX model parameters is

$$\theta(k+1) = a(k)\theta(0) + [1-a(k)]\{\theta(k) + (P(k+1)+Q)\phi(k+1)[R_k + \phi(k+1)^T(P(k+1)+Q)\phi(k+1)]^{-1}(u^*(k+1) - \phi(k+1)\theta(k))\}. \quad (57)$$

The error covariance P is updated by

$$P(k+1) = a(k)P(0) + [1-a(k)]\{(P(k)+Q) - (P(k+1)+Q)\phi(k+1)\phi(k+1)^T + (P(k)+Q)(R_k + \phi(k+1)(P(k)+Q)\phi(k+1))^{-1} + R_1\}, \quad (58)$$

where Q, R_k and R_1 are the pre-set weigthting factors. $a(k) \in (0,1)$ is an algorithm reset, that is, when $a(k) = 1$, $\theta(k)$ and $P(k)$ are reset to their initial values. The error covariance matrix is initialized as $P(0) = \beta I$, where $\beta > 0$.

SIMULATION RESULTS AND DISCUSSION

This section presents the simulation study of side reaction current density estimation using retrospective-cost subsystem identification (RCSI).

The parameters for the electrochemical model are adopted from [17] where the parameters are identified with genetic identification using the cycling data of commercial $LiFePO_4$ batteries. The parameters for battery health model are adopted from [18] where the parameters are identified to produce capacity fade trends that match the manufacturer's cycling and storage data for the same kind of batteries in [17].

The tunable parameters for RCSI are set as follows. The parameters for cost function in retrospective-cost construction part is set as $R_U = 0$ and $R_Z = I_1$. The parameters for Kalman filter updating is set to be $Q = I_1, R_k = 0.5$ and $R_1 = 0$. The estimated parameter is initialized at $\theta(0) = 0$ and the covariance matrix is set at $P(0) = 100I_1$. In the absence of $\hat{E}_2$, Markov parameter is chosen to be $\mathscr{H} = [H_0] = 2 \times 10^{-7}$.

In this paper, an accurate estimation of the battery SoC is assumed. Therefore the initial condition of the system model is set to be exactly the same as the initial states in true system. The effect of measurement noise is also not considered. The model structure presented in previous section contains only the instantaneous impact of the side reaction current density on the output voltage. Because this instantaneous impact is small, the SoH estimation may have a high sensitivity to the SoC estimation error (states error) and noise. This is an area for possible future research.

Next, the simulation results are presented using two types of excitation signals. The first type is constant current discharge and charge cycles. In every cycle, the battery model goes through constant current discharge first and then immediately switches to constant current charge mode. The limit of every cycle is that the SoC is constrained to be between 0.2 and 0.8. The constant voltage modes are eliminated based on the conclusion from [9, 10] where the accurate estimation can be achieved only in constant charge modes. The range of the charge and discharge current for Hybrid Electric Vehicles (HEV) is below 20 C, so the constant current is chosen to be 0.1C and 20C to test the slow charge/discharge and fast charge/discharge cases respectively. Even though the single particle model is accurate only when the input current is below 1 C, the 20 C is used here only to test the effectiveness of RCSI in estimation the side reaction current density. The second type is the current drawn from a battery pack in the vehicle to satisfy the velocity in Urban Dynamometer Driving Schedule (UDDS) test. Because the chemical reaction has relatively slow dynamic, a sampling time of 0.2 second is chosen. The results below also confirm that this sampling rate is fast enough to achieve accurate estimation.

Constant Current Charge and Discharge Cycles

Fig. 4 shows the simulation results of 0.1 C discharge and charge cycle. The sudden drop of the true side reaction current density when switching from discharge mode to charge mode is caused by the sudden change of the current direction (mathematically, the sign of the input flips). Fig. 4 (a) indicates that the estimated side reaction current density starts from zero, but converges to the true value in a short time and keeps tracking the true side reaction current density. Fig. 4 (b) shows the estimated subsystem parameter $\hat{\theta}$ against the true subsystem parameter θ. The estimated parameter $\hat{\theta}$ starts with zero and converges to the true parameter θ very fast. In Fig. 4 (c), the magnified view of the beginning 10 seconds of the operation time is presented. Both $\hat{J}_{sd}$ and $\hat{\theta}$ converge to the true values in less than 10 seconds.

Fig. 5 shows the simulation results of four 20 C discharge and charge cycles. Fig. 5 (a) shows that the estimated side reaction current density $\hat{J}_{sd}$ can track the true side reaction current density J_{sd} during the whole cycle. Fig. 5 (b) shows that the estimated subsystem parameter $\hat{\theta}$ converges to the true value very fast during the constant current charge mode. But $\hat{\theta}$ cannot track the true value during the constant current discharge mode. Even during the second to four cycle, when the subsystem parameter θ is correctly estimated by $\hat{\theta}$ during the constant current charge mode in the previous cycle, $\hat{\theta}$ will diverge from θ after switching to constant current discharge mode.

This result agrees with the analysis of the true system, where the side reaction current density is near zero under a high discharge C rate. Under a discharge rate of 20 C, the side reaction current density is less than 0.5 A/m^3. This result agrees with the assumption in [2] where the degradation in discharge phase is negligible. As a result, the impact of the subsystem output on the output voltage is negligible, hence weak identifiability of the subsystem parameter under a high discharge C rate. However, for the side reaction current density, as long as the input to the subsystem remains small, the error in the estimated subsystem parameter does not cause a large error in estimated side

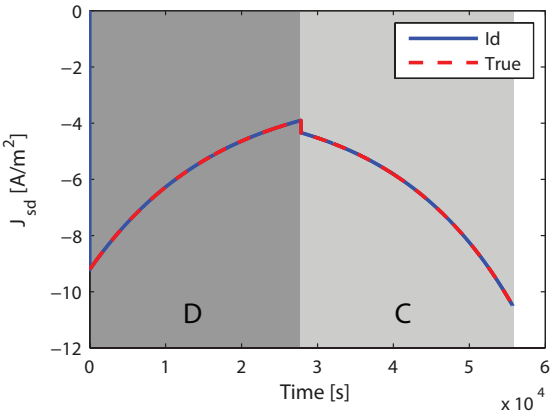

(a) Estimated side reaction current density $\hat{J}_{sd}$.

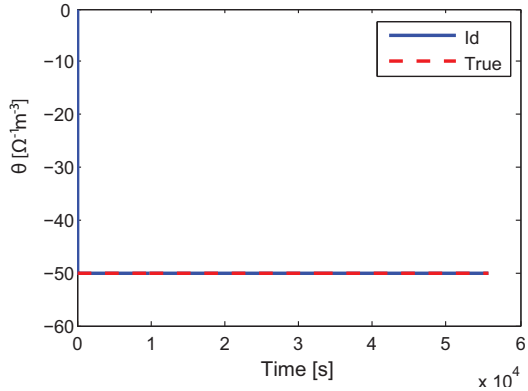

(b) Estimated subsystem parameter $\hat{\theta}$.

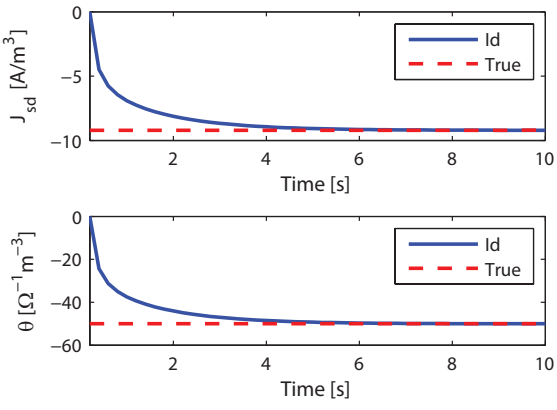

(c) Magnified view of the beginning section of the estimated $\hat{J}_{sd}$ and $\hat{\theta}$.

FIGURE 4. Estimated results with 0.1 C constant current discharge and charge cycle. The red dash lines denote the true value while the blue lines denote the estimated value. Area denoted with D is the constant current discharge mode; area denoted with C is the constant current charge mode. This case shows that estimation result in slow charge and discharge case.

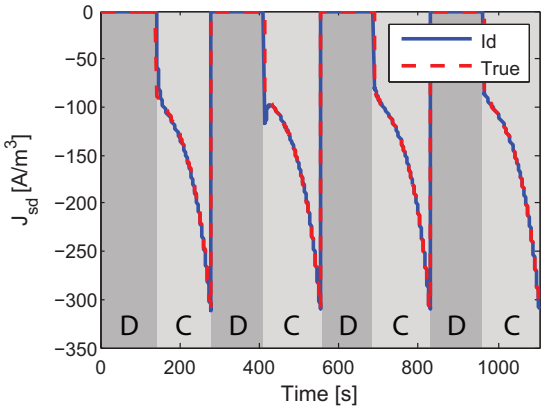

(a) Estimated side reaction current density $\hat{J}_{sd}$.

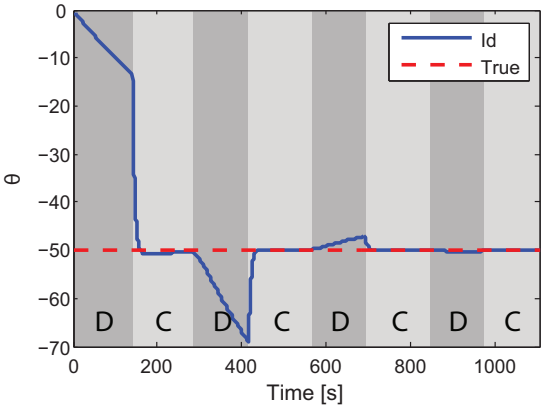

(b) Estimated subsystem parameter $\hat{\theta}$.

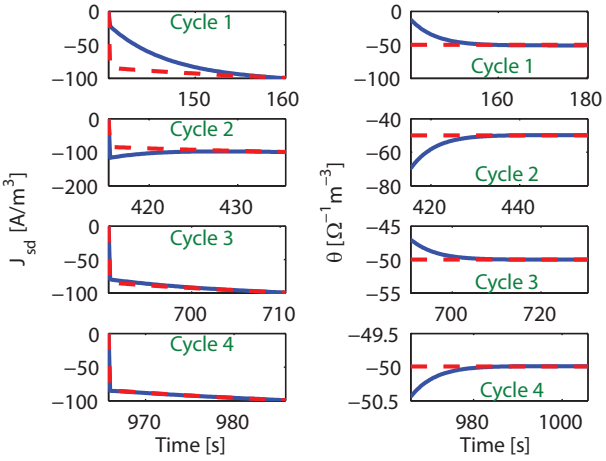

(c) Magnified view of the estimated $\hat{J}_{sd}$ and $\hat{\theta}$ in the beginning of the charge mode in every cycle.

FIGURE 5. Estimated results with 20 C constant current discharge and charge cycle. The red dash lines denote the true value while the blue lines denote the estimated value. Area denoted with D is the constant current discharge mode; area denoted with C is the constant current charge mode. This case shows that estimation result in fast charge and discharge case.

reaction current density. The accurate estimation of side reaction current density is just an artefact of near zero subsystem input. This conclusion also agrees with the conclusion in [9, 10]. Fig. 5 (c) shows the magnified view of the estimated $\hat{J}_{sd}$ and $\hat{\theta}$ during every constant current charge mode. The estimated subsystem parameter $\hat{\theta}$ converges to the true value in less than 40 seconds after switching to charge mode. However, the estimated $\hat{\theta}$ in constant current discharge modes is also approaching the true value with cycle number growing. Because the estimated $\hat{\theta}$ in constant current charge modes in the previous cycles is closer to the true value as shown in Fig. 5 (c) when comparing the estimated $\hat{\theta}$ from up (cycle 1) to down (cycle 4), the initial $\hat{\theta}$ value in every discharge mode is nearer to the true value than the previous discharge mode and hence the divergence is less pronounced.

UDDS Test Cycles

Fig. 6 shows the estimation result with the simulation current profile of an electric vehicle (EV) battery to satisfy one Urban Dynamometer Driving Schedule (UDDS) cycle. This current profile is generated from Advisor software [19] with the default EV setting. The default setting of the Li-ion battery in Advisor is about 7 Ah, while the rated capacity of the battery model in this paper is 2.3 Ah. The current magnitude is scaled down accordingly to match the C rate and ensure that the battery is not overcharged.

Fig. 6 (a) shows that the estimated side reaction current density $\hat{J}_{sd}$ during the whole cycle. $\hat{J}_{sd}$ starts from zero and converges to the true J_{sd} very fast. J_{sd} estimation error is the percentage difference between estimated J_{sd} and true J_{sd}. The subplot below shows that the J_{sd} estimation error after 40 seconds (after the estimated θ converges near the true value) is below 0.8%. Fig. 6 (b) shows that the estimated subsystem parameter $\hat{\theta}$. $\hat{\theta}$ starts from zero and converges to the true θ very fast. The estimated parameter contains some fluctuation during the time when the true J_{sd} is small and the degradation is negligible. This agrees with the results shown in the previous subsection where the estimated parameter $\hat{\theta}$ diverges from the correctly estimated parameter when the degradation becomes insignificant. The subplot below shows that the estimation error of θ after 40 seconds is below 0.8%. In this paper, the relative error between $\hat{J}_{sd} = \hat{\theta}\hat{y}$ and $J_{sd} = \theta y$ and that between $\hat{\theta}$ and θ resemble each other because $\hat{y}$ and y are close in the simulation. Fig. 6 (c) shows the magnified view of the beginning section of the estimated side reaction current density and parameter. Both estimations converge to their true values in 8 seconds. This result reveals that RCSI can estimate both side reaction current density and subsystem parameter effectively with the dynamic current profile in EV operating condition.

CONCLUSION

In this paper, the effectiveness of retrospective-cost subsystem identification (RCSI) in estimation of the side reaction current density is explored. The side reaction current density is consid-

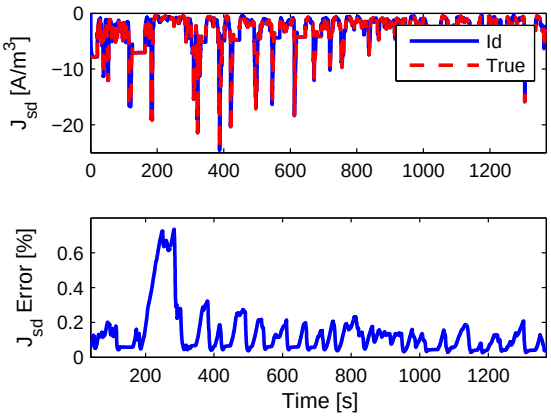

(a) Estimated side reaction current density $\hat{J}_{sd}$.

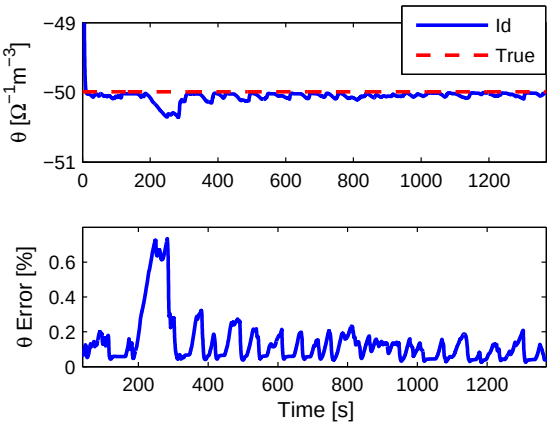

(b) Estimated subsystem parameter $\hat{\theta}$.

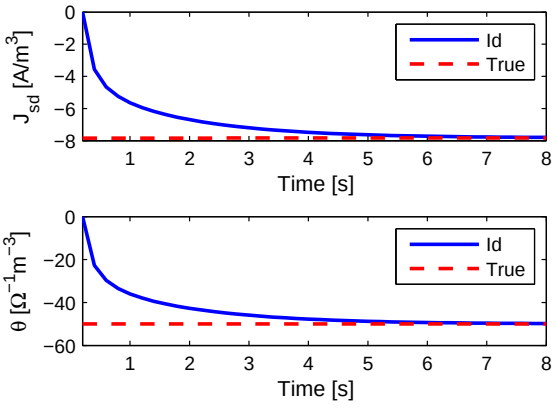

(c) Magnified view of the mode transition section of the estimated $\hat{J}_{sd}$ and $\hat{\theta}$.

FIGURE 6. Estimated results with one UDDS cycle. The red dash lines denote the true value while the blue lines denote the estimated value. This case modelled the current dynamic requirement for the battery during the operation of electric vehicles.

ered for the first time to be the SoH indicator. Under the assumption of accurate knowledge of SoC and no measurement noise, the result of this paper shows that retrospective-cost subsystem identification (RCSI) can accurately and quickly estimate the side reaction current density when the degradation effect is significant. The accurate estimation can be made during the whole operating time of slow constant current charge and discharge cycle (0.1 C) and UDDS Test (below 0.8%). During fast constant current charge and discharge cycles (20 C), RCSI can accurately estimate the side reaction current density during constant current charge mode when the sampling time is fast enough. In this paper, an accurate SoC estimation is assumed and no noise is considered. Future investigation will include the techniques to reduce the sensitivity to SoC estimation error and noise.

ACKNOWLEDGMENT

This material is based upon work supported by China-US Clean Energy Research Center. Acknowledgement to Gerardo Cruz and Ray Yu for providing the RCSI Matlab code.

REFERENCES

[1] Arora, P., White, R. E., and Doyle, M., 1998. "Capacity fade mechanisms and side reactions in lithium-ion batteries". *Journal of the Electrochemical Society,* **145**(10), pp. 3647–3667.

[2] Ramadass, P., Haran, B., Gomadam, P. M., and White, R. E., 2004. "Development of first principles capacity fade model for li-ion cells". *Journal of the Electrochemical Society,* **151**, February, pp. A196–A203.

[3] Plett, G. L., 2004. "Extended kalman filtering for battery management systems of lipb-based hev battery packs: Part 1. background". *Journal of Power sources,* **134**(2), pp. 252–261.

[4] Plett, G. L., 2004. "Extended kalman filtering for battery management systems of lipb-based hev battery packs: Part 2. modeling and identification". *Journal of power sources,* **134**(2), pp. 262–276.

[5] Plett, G. L., 2004. "Extended kalman filtering for battery management systems of lipb-based hev battery packs: Part 3. state and parameter estimation". *Journal of Power sources,* **134**(2), pp. 277–292.

[6] Remmlinger, J., Buchholz, M., Soczka-Guth, T., and Dietmayer, K., 2013. "On-board state-of-health monitoring of lithium-ion batteries using linear parameter-varying models". *Journal of Power Sources,* **239**(0), pp. 689 – 695.

[7] Vetter, J., Novak, P., Wagner, M., Veit, C., Möller, K.-C., Besenhard, J., Winter, M., Wohlfahrt-Mehrens, M., Vogler, C., and Hammouche, A., 2005. "Ageing mechanisms in lithium-ion batteries". *Journal of power sources,* **147**(1), pp. 269–281.

[8] Moura, S. J., Krstic, M., and Chaturvedi, N. A., 2012. "Adaptive pde observer for battery soc/soh estimation". In ASME 2012 5th Annual Dynamic Systems and Control Conference, American Society of Mechanical Engineers, pp. 101–110.

[9] D'Amato, A. M., Forman, J. C., Ersal, T., Ali, A. A., Stein, J. L., Peng, H., and Bernstein, D. S., 2012. "Noninvasive battery-health diagnostics using retrospective-cost identification of inaccessible subsystems". In ASME 2012 5th Annual Dynamic Systems and Control Conference, American Society of Mechanical Engineers, pp. 299–307.

[10] Zhou, X., Ersal, T., Stein, J. L., and Bernstein, D. S., 2013. "Battery health diagnostics using retrospective-cost system identification: Sensitivity to noise and initialization errors". In ASME 2013 6th Annual Dynamic Systems and Control Conference, p. 3953 (10 pages).

[11] Morozov, A. V., Ali, A. A., D'Amato, A. M., Ridley, A. J., Kukreja, S. L., and Bernstein, D. S., 2011. "Retrospective-cost-based model refinement for system emulation and subsystem identification". In Decision and Control and European Control Conference (CDC-ECC), 2011 50th IEEE Conference on, IEEE, pp. 2142–2147.

[12] D'Amato, A. M., Ridley, A. J., and Bernstein, D. S., 2011. "Retrospective-cost-based adaptive model refinement for the ionosphere and thermosphere". *Statistical Analysis and Data Mining,* **4**(4), pp. 446–458.

[13] Doyle, M., Fuller, T. F., and Newman, J., 1993. "Modeling of galvanostatic charge and discharge of the lithium/polymer/insertion cell". *Journal of the Electrochemical Society,* **140**(6), pp. 1526–1533.

[14] Santhanagopalan, S., Guo, Q., Ramadass, P., and White, R. E., 2006. "Review of models for predicting the cycling performance of lithium ion batteries". *Journal of Power Sources,* **156**, pp. 620–628.

[15] Forman, J. C., Bashash, S., Stein, J. L., and Fathy, H. K., 2011. "Reduction of an electrochemistry-based li-ion battery model via quasi-linearization and pade approximation". *Journal of the Electrochemical Society,* **158**, February, pp. A93–A101.

[16] Di Domenico, D., Stefanopoulou, A., and Fiengo, G., 2010. "Lithium-ion battery state of charge and critical surface charge estimation using an electrochemical model-based extended kalman filter". *Journal of Dynamic Systems, Measurement, and Control,* **132**(6), p. 061302 (11 pages).

[17] Forman, J. C., Moura, S. J., Stein, J. L., and Fathy, H. K., 2012. "Genetic identification and fisher identifiability analysis of the doyle-fuller-newman model from experimental cycling of a lifepo4 cell". *Journal of Power Sources,* **210**, July, pp. 263–275.

[18] Bashash, S., Moura, S. J., Forman, J. C., and Fathy, H. K., 2011. "Plug-in hybrid electric vehicle charge pattern optimization for energy cost and battery longevity". *Journal of Power Sources,* **196**(1), pp. 541 – 549.

[19] Brooker, A., and et al. Advanced vehicle simulator. `http://adv-vehicle-sim.sourceforge.net`.